

Article

Optimal Design of IPMSM for FCEV Using Novel Immune Algorithm Combined with Steepest Descent Method

Ji-Chang Son, Young-Rok Kang and Dong-Kuk Lim *

School of Electrical Engineering, University of Ulsan, Ulsan 44610, Korea; wlckd1116@naver.com (J.-C.S.); myduddk77@gmail.com (Y.-R.K.)

* Correspondence: ldk8745@ulsan.ac.kr; Tel.: +82-52-259-1072

Received: 28 April 2020; Accepted: 28 June 2020; Published: 2 July 2020



Abstract: In this paper, the Novel Immune Algorithm (NIA) is proposed for an optimal design of electrical machines. By coupling the conventional Immune Algorithm and Steepest Descent Method, the NIA can perform fast and exact convergence to both global solutions and local solutions. Specifically, the concept of an antibody radius is newly introduced to improve the ability to navigate full areas effectively and to find new peaks by excluding already searched areas. The validity of the NIA is confirmed by mathematical test functions with complex objective function regions. The NIA is applied to an optimal design of an interior permanent magnet synchronous motor for fuel cell electric vehicles and to derive an optimum design with diminished torque ripple.

Keywords: fuel cell electric vehicle (FCEV); interior permanent magnet synchronous motor (IPMSM); multi-modal optimization; Novel Immune Algorithm (NIA); optimal design

1. Introduction

Recently, as the problems of energy crisis and environmental pollution have become more serious, electric vehicles, such as fuel cell electric vehicles (FCEVs), are an increasing portion of the market, as they are cleaner than conventional internal combustion engine vehicles [1,2]. As FCEVs require high-power density and high efficiency, the interior permanent magnet synchronous motor (IPMSM) has been widely used for motors for FCEVs [3–5]. IPMSM is a motor in which permanent magnets are embedded in the rotor core. Owing to such structural characteristics, the IPMSM has either higher average torque or superior performance at high speed compared with a surface-mounted permanent magnet synchronous motor [6,7].

An engineer should design a motor for FCEV to have lower torque ripple for the purpose of comfortable driving and improved control stability, because torque ripple causes vibration and noise in the motor [8,9]. Therefore, this paper aims at the optimal design of an IPMSM for FCEVs to have lower torque ripple and satisfying rated torque.

The performance of an IPMSM can be improved by optimizing the design of the permanent magnet structure, and the objective function of torque ripple has a complex shape with many local minima. To analyze the load condition of the IPMSM accurately, the finite element method (FEM) is needed, as the IPMSM has nonlinear magnetic saturation [10]. However, the FEM requires an enormous amount of time and effort, especially when applied to search multiple peaks at multi-modal problems.

To address this problem, the conventional Immune Algorithm (IA), which mimics the human immune system, was devised [11]. However, like other stochastic algorithms, the IA needs many function calls and iterations to find the accurate peak. To resolve problems regarding computational cost, this paper proposes a Novel Immune Algorithm (NIA). The NIA is a hybrid algorithm that consists

of the conventional IA and the Steepest Descent Method (SDM), which is a kind of deterministic method. In addition, the concept of an antibody radius is newly adopted for conventional IA, enhancing the ability to search entire areas efficiently. As a result, the NIA can significantly reduce the number of function calls to find multiple peaks accurately.

The NIA, conventional IA, and Niching Genetic Algorithm (NGA) were applied to two mathematical test functions with many local peaks, and the outstanding performance of the NIA was validated by comparison with the IA and NGA results. Finally, the proposed algorithm was applied to an optimal design of an IPMSM for FCEVs and to derive an optimum design that minimizes torque ripple and satisfies the rated torque and low cogging torque.

2. Conventional Immune Algorithm

The human immune system detects invading antigens such as viruses or germs that enter the human body and remove antigens by generating antibodies corresponding to the antigens. The IA is an algorithm that mimics this system, and it is applied for the optimization of the objective function. Among the many stochastic algorithms, the IA shows superior performance when applied to complex optimization problems with multiple local solutions [12]. Hence, this paper proposes an algorithm that is based on the IA. The IA accomplishes optimization using concepts such as antibody, memory cell, affinity, and expectation. The flow chart of the IA is shown in Figure 1, and the flow of the IA is described below.

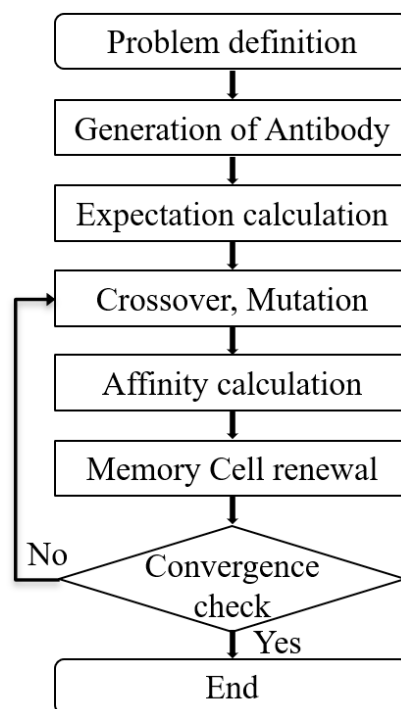


Figure 1. Flow chart of the conventional immune algorithm.

1. Problem definition: Objective function and restrictions are defined.
2. Generation of antibody: Initial antibodies are generated randomly in the problem region and initial memory cells are selected according to antibody-antigen affinity. When the algorithm is applied to find peaks, the antibody-antigen affinity of an antibody (v) is defined as follows:

$$aff_v = cur_v \quad (1)$$

If the aim of the algorithm is minimization, antibody-antigen affinity is defined as:

$$aff_v = -cur_v \quad (2)$$

where cur_v is the objective function value.

- Expectation calculation: The expectation of each antibody is calculated and antibodies with low expectations are removed. The expectation of antibody (i) is calculated as follows:

$$e_i = aff_i/c_i \quad (3)$$

where c_i is the concentration, which is defined as the number of antibodies having the similar value as antibody (i), divided by the total number of antibodies. Figure 2 and Table 1 show how expectation works in the algorithm. When the value of B and D is considered as similar, the concentration of A and C is low, and concentration of B and D is relatively high. Therefore, the expectation is calculated as listed in Table 1, and you can figure out that the local peak A is more likely to survive than B or D.

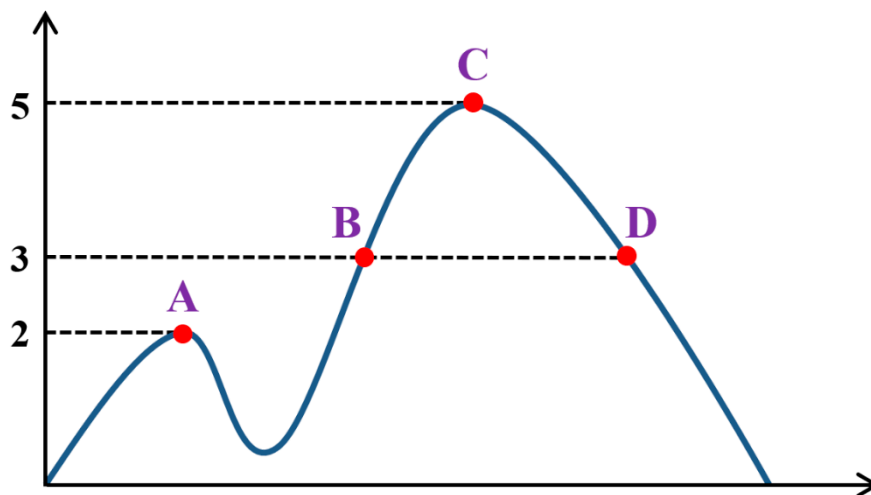


Figure 2. Example of calculating concentration and expectation.

Table 1. Calculation result of concentration and expectation.

Point	Concentration	Expectation
A	1/4	$2 \times 4/1 = 8$
B	2/4	$3 \times 4/2 = 6$
C	1/4	$5 \times 4/1 = 20$
D	2/4	$3 \times 4/2 = 6$

- Crossover, mutation: The antibody group is updated by replacing removed antibodies. Mutants are randomly generated in the entire problem area and crossover is done by the antibodies remaining from step 3.
- Affinity calculation: The antibody-antigen affinity of the new antibody group is calculated with (3). Additionally, the antibody-antibody affinity of the memory cell is calculated as follows:

$$aff_{v,w} = 1/(1 + dist_{v,w}) \quad (4)$$

where $dist_{v,w}$ is the distance between newly generated antibody (v) and antigen (w). Antigens are entities involved in the memory cells. With this step, antibodies near the memory cells are candidates of elimination, enhancing the ability to find unknown areas.

6. Memory cell renewal: Cells with high antibody-antibody affinity in memory cells are removed, and antibodies with high antibody-antigen affinity are added to the memory cell.
7. Convergence check: If the value of the memory cell group is not changed by N iteration, it is judged that the convergence condition is satisfied, and the algorithm terminates and the optimal solutions are saved to the memory cell. If the convergence condition is not satisfied, each step is repeated from step 4, and the algorithm proceeds.

3. Proposed Algorithm

Even though the conventional IA performs better in multi-modal optimization problems than other heuristic algorithms, the IA also has a problem that requires many function calls to converge to an accurate peak like other stochastic algorithms. To address the problem with computational cost, the NIA is proposed. The NIA improves the performance of the conventional IA using three concepts.

3.1. Multi-Jittered Sampling

As shown in Figure 3a, a conventional IA generates initial solutions randomly in the problem domain. The NIA adopts Multi-Jittered Sampling (MJS) to generate initial solutions. At first, the MJS divides the problem region into $N \times M$ subregions, and generates one sample for each subregion. In Figure 3b, the red lines divide the problem region into subregions and only one sample exists in each subregion, where N and M are both 4. The subregions are subdivided into $N \times M$ grid, marked with black lines, to place only one sample in one subregion. Additionally, there are no other samples in each row and column. In other words, initial samples are scattered throughout the entire region and have randomness too, enhancing the ability to find local minima. By adopting the MJS method, a more superior set of initial samples can be obtained, compared with the conventional method of generating samples on the entire region randomly.

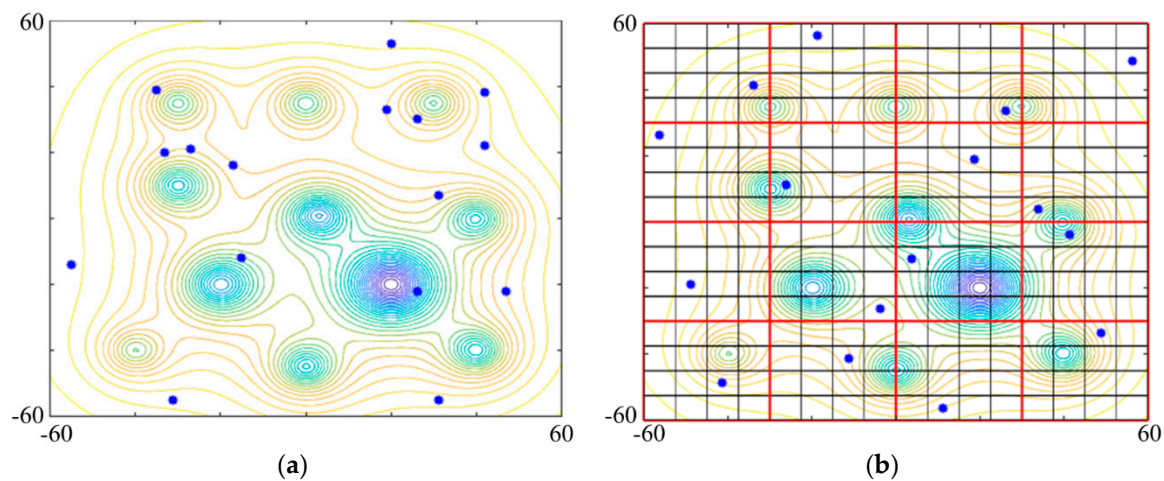


Figure 3. Example of sampling: (a) Random sampling; (b) Multi-Jittered sampling.

3.2. Hybrid Steepest Descent Method

The IA, which is a kind of stochastic optimization method, can find global and local solutions. However, the IA requires a lot of function calls to converge to an accurate optimal solution. On the other hand, the SDM, one of the deterministic optimization methods, finds the exact optimal solution quickly using gradient information along the search direction. However, in the complex objective function domain with many local minima, the SDM has the problem of premature convergence to a local solution, instead of a global solution [13]. The NIA combines the SDM with the IA to compensate for the shortcomings and maximize the advantages. The SDM is applied to memory cells and new antibodies, allowing them to converge directly to local peaks nearby. As a result, the NIA can find

accurate peaks with a remarkably reduced number of function calls and can search both global and local solutions.

3.3. Antibody Radius

The NIA utilizes the concept of an antibody radius to maximize its ability to navigate unexplored area. The antibody radius is the distance between a memory cell and the closest memory cell. New antibodies, or mutations, are generated outside the antibody radius and the radius is adjusted automatically when a new memory cell is added.

Figure 4 intuitively shows how the new antibody is added and how the antibody radius is adjusted. On the left, there is a memory cell with the antibody radius set beforehand, and the new antibody is generated outside the circle. Using the SDM, the new antibody converges to the peak nearby and the antibody radius is adjusted automatically.

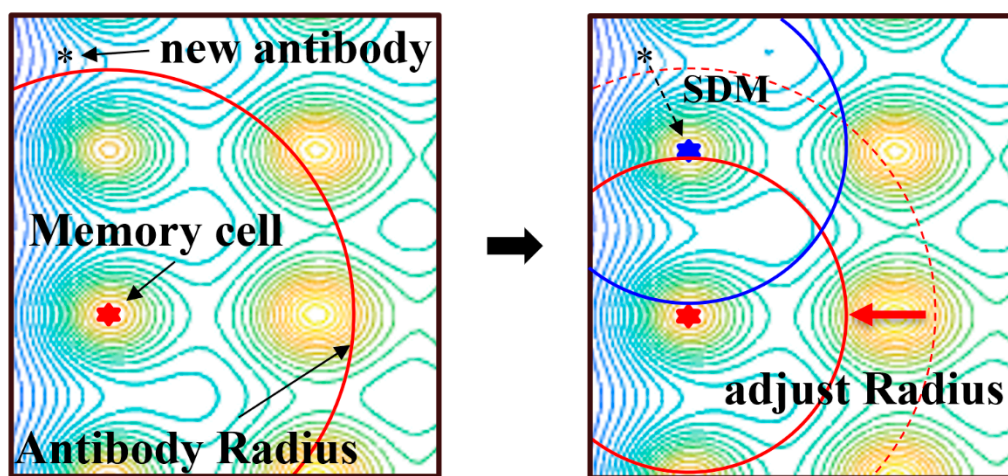


Figure 4. Conceptual schematic of the Novel Immune Algorithm (NIA) showing how the antibody radius is adjusted.

3.4. Flow Chart of the NIA

The flow chart of the NIA is shown in Figure 5. First, the objective function and constraints are defined, and initial samples are created using MJS. The red box shows how the antibody group is updated as the algorithm progresses. Among the initial samples, antibodies with high value are added to the memory cell group. The antibody-antibody affinity of the antibody group is calculated with “(4)” and low affinity antibodies are removed. Then the expectation is calculated according to “(3)” and high expectation antibodies are differentiated into the memory cell group.

The blue box is the part that handles the memory cell group. Initial memory cells or newly differentiated memory cells find local peaks using the SDM. If a new peak is found, it is added to the memory cell. If it converges to a peak that has already been found, it is removed. The antibody radius is automatically adjusted to the distance from the nearest memory cell. If the convergence condition is not satisfied, the antibodies with high expectations are added to the memory cell, and the algorithm is repeated.

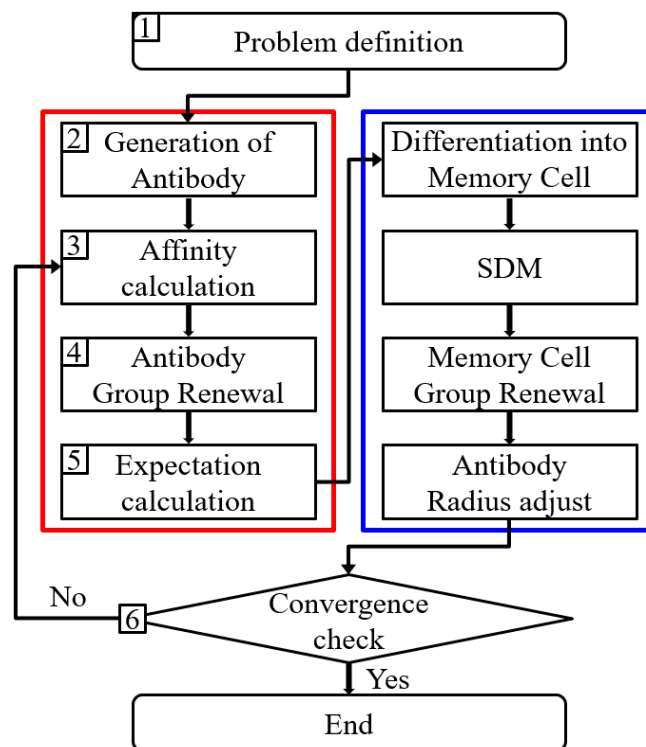


Figure 5. Flow chart of the Novel Immune Algorithm.

3.5. Verification of the Proposed Algorithm

In order to verify the reliability and superiority of the algorithm, conventional IA, NGA, and the NIA are applied to the optimization of two mathematical functions. Test function 1 is defined as follows:

$$f_1(x, y) = \sum_{i=1}^{np_1} \frac{b_i}{1 + [(x - x_i)^2 + (y - y_i)^2]/a_i} \quad (5)$$

and test function 2 is given as:

$$f_2(x, y) = \sum_{k=1}^{np_2} \frac{60}{1 + [(x - x_k)^2 + (y - y_k)^2]/a_k} \quad (6)$$

where (x_i, y_i) and (x_k, y_k) are the coordinates of the peaks of the test functions, and a_i , a_k , and b_i are the values related to the magnitude of the peaks. np_1 and np_2 are the values that determine the number of peaks of each function and the values are 11 and 36, respectively. As shown in Figure 6, the two test functions have complex objective domains with 11 and 36 peaks, respectively. The test was repeated 100 times in total and it was judged to be successful when the found peak rates were more than 95% of the actual peak value. The test results are listed in Table 2. As the NIA combines with the deterministic method, SDM, it shows a tremendous improvement in the success rate compared to the conventional IA. In terms of the number of function calls, the NIA is superior to the IA, as the NIA generates samples effectively considering the antibody radius. Moreover, the NIA seems to be superior compared with the NGA, as the NIA adjusts the radius automatically. It is obvious that the NIA shows outstanding performance in both accuracy and computational cost, compared with a conventional IA and NGA.

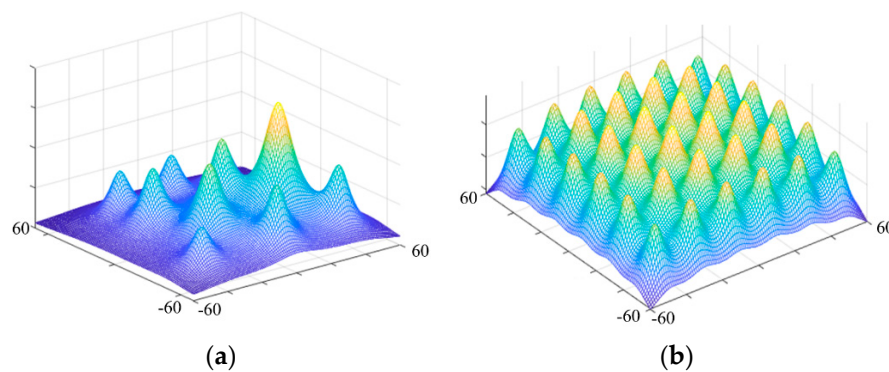


Figure 6. Three-dimensional plot of test functions: (a) Test function 1 with 11 peaks; (b) Test function 2 with 36 peaks.

Table 2. Performance comparison between the NIA, IA, and NGA.

Test Function 1 [11 Peaks]	Number of Function Call	Success Rate [%]
IA	2060.0	58.45
NGA	1650	89.09
NIA	1365.2	99.45
Test Function 2 [36 Peaks]	Number of Function Call	Success Rate [%]
IA	3390.0	84.0
NGA	3140	94.44
NIA	1878.1	99.64

4. Application to the Optimal Design of IPMSM for FCEV

4.1. Analysis Model and Design Variables

Electrical vehicles have been increasing as a portion of the commercial market over the past few decades for the purpose of reducing air pollution in cities [14]. For the commercialization of FCEVs, high torque density and efficiency are required to increase the power transmission and the saving of energy because the motors solely drag a car without the engine and only use the energy from a battery [15]. The IPMSM is selected as the model for the FCEV motor, because the IPMSM has the advantages of high torque density and efficiency [16,17]. However, due to saliency, the IPMSM suffers from high torque ripple, causing undesired noise and vibration during its operation and reducing driving impression and control stability [18]. As a motor for FCEVs should have lower torque ripple, the purpose of design is to diminish torque ripple [19].

Torque ripple of IPMSM can be reduced depending on the shape of the rotor or placement of the permanent magnets [20,21]. Therefore, as shown in Figure 7, the design variables are determined as the angle of each magnet and the length between two magnet layers to change the shape of the permanent magnets inside the rotor core. The values related to the rest of the shape are fixed and set the constraints that the magnets are not deviated from the rotor core and the magnets in each layer are not overlapped. The length of the bridge and center post are kept uniform in order to guarantee mechanical stability, even if design parameters are changed. Detailed specifications and requirements of an objective motor are listed in Table 3, and the available range of each variable is indicated in Table 4. In detail, the number of poles and slots of the initial model is 6 and 27, respectively. The rotor has a multipolar structure and a multi-layered magnet to satisfy the high-power density and high torque density requirements of FCEVs. For the stator, the number of slots was selected through cogging torque comparison of the other pole and slot combinations [22]. For the practical design, parameters that related to structure of the stator and rotor were selected according to [22].

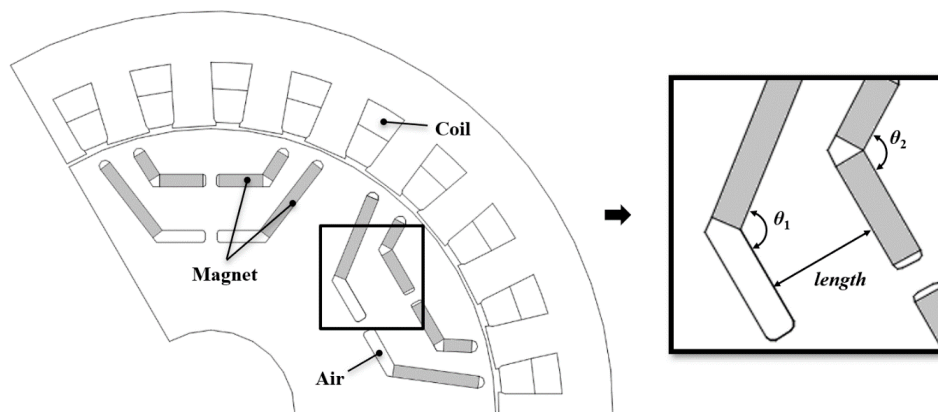


Figure 7. One-third of the periodic analysis model of basic model and design variables.

Table 3. Specifications and requirements of an objective motor.

Parameter	Unit	Value
Pole number	-	6
Slot number	-	27
Rated torque	[Nm]	310
Rated power	[kW]	97.4
Rotation speed	[rev/min]	3000
Stator inner/outer diameter	[mm]	172/240
Rotor inner/outer diameter	[mm]	50/170
Air gap	[mm]	1
Stacking length	[mm]	240
Stator and rotor core material	-	JFE steel 35JN230
Permanent magnet material	-	NEOMAX-42

Table 4. Range of design variables.

Variable	Unit	Range
θ_1	[degree]	125–140
θ_2	[degree]	100–150
$length$	[mm]	12–18.5

The proposed NIA is applied for an optimal design of the IPMSM for FCEVs. Whenever new antibodies are generated in the algorithm, shape design of the IPMSM reflecting each parameter value is performed and the FEM, using an analysis tool, is executed to obtain results.

For the IPMSMs, the magnitude of the average torque changes with the current phase angle. Figure 8 shows the average torque of the initial model and the current phase angle is changed in 2° intervals from 0° to 90° . When the rotor shape of an IPMSM is changed, the current phase having maximum average torque changes. Therefore, the algorithm is set to find the current phase with maximum torque whenever the design changes.

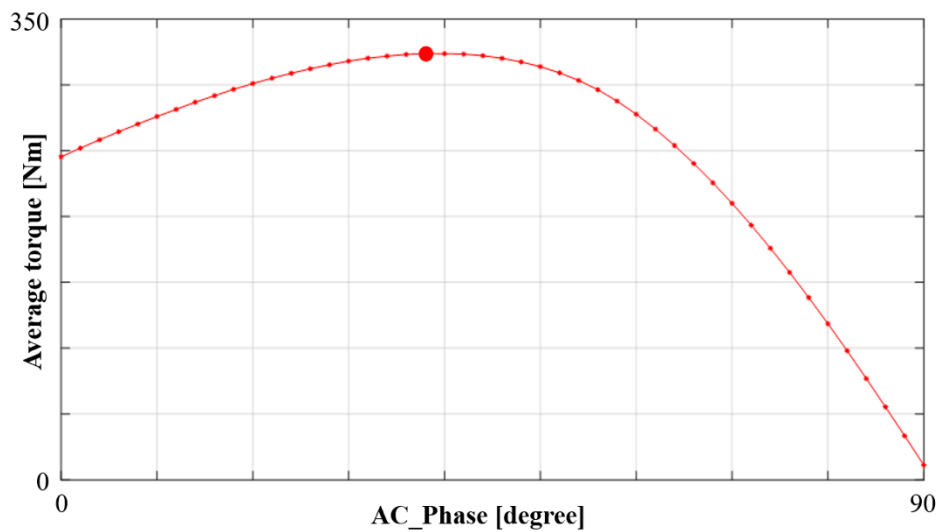


Figure 8. Comparison of average torque of the initial model according to the current phase angle.

4.2. Optimization Results

By applying FEM analysis to the NIA, three optimal models with diminished torque ripple are derived. Figure 9 shows the objective region, which is torque ripple, according to the variables and has nonlinear shape with multiple solutions. The final design is selected considering not only torque ripple but also average torque and cogging torque. In Table 5, the obtained values of design variables for the initial and the candidate models are listed. Table 6 numerically shows torque ripple, average torque, cogging torque, and current phase having maximum torque of each model.

In detail, in terms of torque ripple, model 1 is a better design than the other candidates and it also has a relatively low cogging torque. However, model 1 does not meet the rated torque requirement. Model 2 has a relatively small torque ripple and the highest average torque, but its cogging torque value is too high. Model 3 seems to be the most suitable design when considering torque ripple, average torque, and cogging torque. Therefore model 3 is decided as the optimum design.

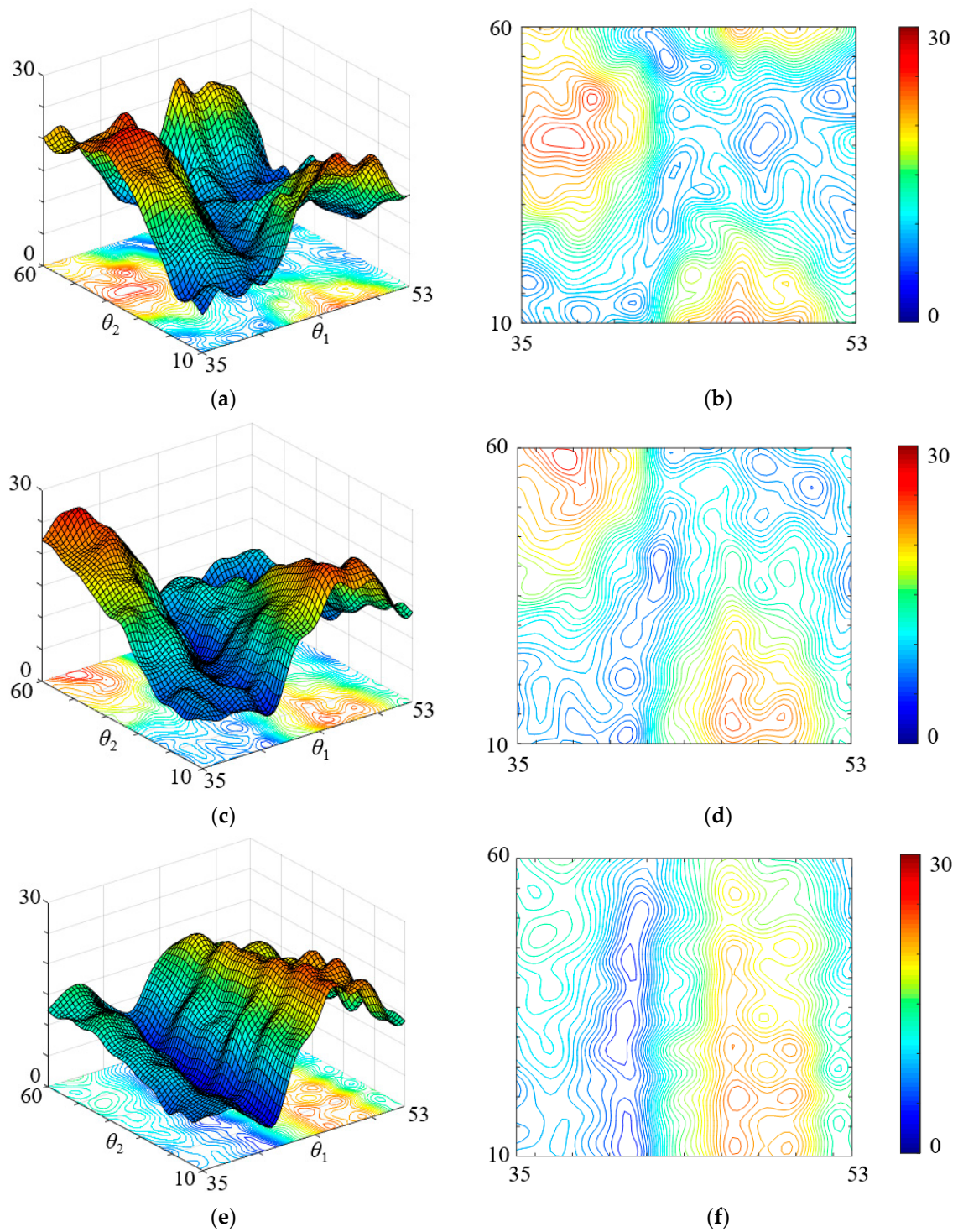


Figure 9. Torque ripple for design variable θ_1 and θ_2 : (a) 3-Dimensional plot when *length* is 13 mm; (b) Contour plot when *length* is 13 mm; (c) 3-Dimensional plot when *length* is 15.5 mm; (d) Contour plot when *length* is 15.5 mm; (e) 3-Dimensional plot when *length* is 18 mm; (f) Contour plot when *length* is 18 mm.

Table 5. Variables of initial and optimal models.

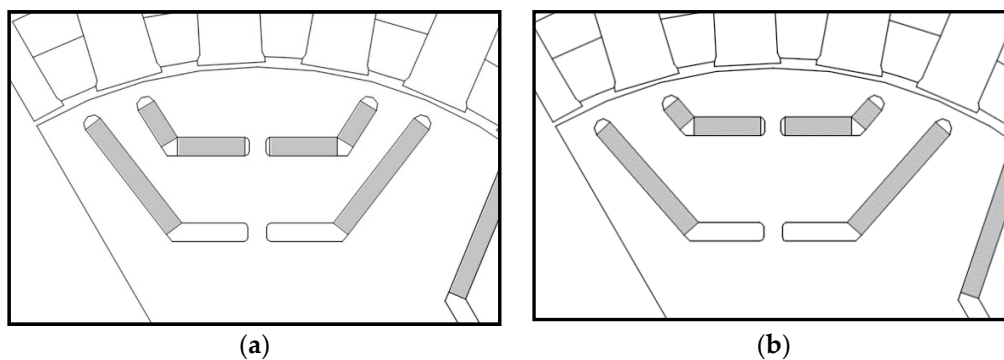
Model	Initial Model	Model 1	Model 2	Model 3
θ_1 [degree]	127.67	130.77	141.50	131.33
θ_2 [degree]	122.22	111.33	124.00	130.08
length [mm]	13.0	18.5	12.0	17.0

Table 6. Performance comparison of initial and optimal models.

Model	Initial Model	Model 1	Model 2	Model 3
Torque Ripple [%]	19.58	2.68	4.10	4.36
Average Torque [Nm]	322.39	304.97	323.71	315.49
Cogging Torque [Nm]	24.11	6.23	21.52	2.92
AC phase [degree]	43	45	39	44

4.3. Result Analysis of Optimum Design

Figure 10 shows the permanent magnet structure of initial and optimum design of the IPMSM. Magnet usage of the optimum model is 6.4% lower than the initial model, however, the average torque is only 2% smaller than the initial model. Figure 11a shows the torque waveform of the initial model and optimized model. The average torque of the initial model is 322.39 Nm, and of the optimized model is 315.49 Nm, which is reduced by 2.1% compared to the initial model. However, the torque ripple of the optimized model is decreased by 77.73% compared to the initial model, with the optimal model being 4.36% and the initial model being 19.58%. Figure 11b shows the cogging torque comparison between the initial model and optimum model. The cogging torque of the initial model is 24.11 Nm and of the optimized model is 2.92 Nm, which is 87.89% less than the initial model.

**Figure 10.** Permanent magnet structure: (a) Initial model; (b) Optimum model.

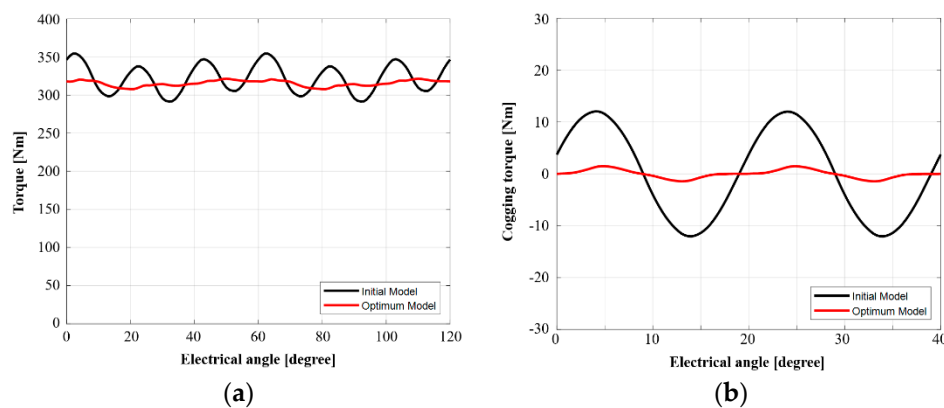


Figure 11. Waveform comparison of the initial model and optimum model: (a) Torque waveform; (b) Cogging torque waveform.

The magnetic flux density of the optimum models is displayed in Figure 12. The maximum values of the initial model and optimum model are 2.61 T and 2.47 T, respectively, and the optimum model shows 22.95% lower saturation than that of the initial model. Table 7 represents power characteristics of both models, and there is no difference for the efficiency.

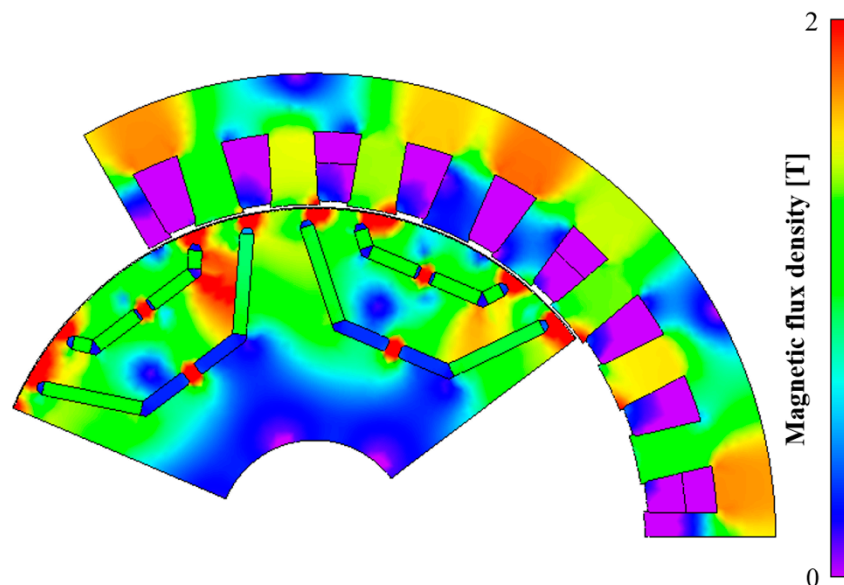


Figure 12. Magnetic flux density of the optimum model.

Table 7. Power characteristics of the initial model and optimum model.

Model	Initial Model	Optimum Model
Iron loss [W]	507.8	473.5
Copper loss [W]	2162.7	2162.7
Total loss [W]	2670.5	2636.1
Input power [kW]	103.9	101.7
Output power [kW]	101.3	99.1
Efficiency [%]	97.4	97.4

For the IPMSM, bilateral and central bridges suffer maximum mechanical stress and are most vulnerable to breakage during high-speed rotation [23,24]. Therefore, analysis of mechanical stress at high speed should be considered when designing the IPMSMs. Table 8 shows parameters of mechanical stress analysis. Maximum rotational speed of the rotor is set as 6000 rpm, which is twice

the rated rotation speed, to ensure stability against breakage at high speed. Figure 13 shows the result of mechanical stress analysis at the maximum speed. The maximum Von Mises stress of maximum speed and rated speed are 114.74 MPa and 28.5 MPa, respectively. The results show that the optimal design does not exceed the yield stress value of 230 MPa, and is safe from breakage even at high speed.

Table 8. Setting for the mechanical stress analysis.

Parameter	Value
Young's modulus (Core/PM)	210/120 [GPa]
Poisson's ratio (Core/PM)	0.3/0.3
Density (Core/PM)	7850/8400 [kg/m ³]
Rotation speed	3000/6000 [rpm]
Yield stress	250 [MPa]

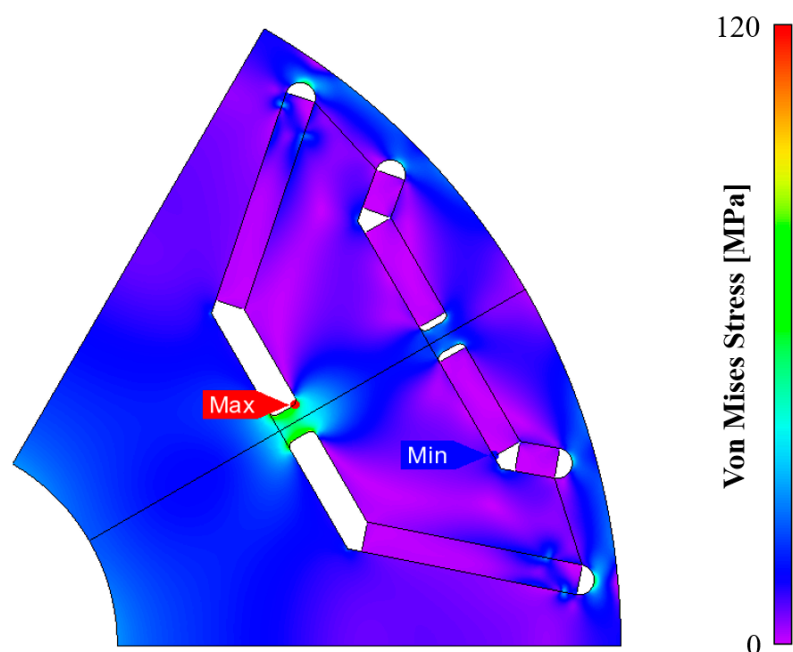


Figure 13. Von Mises stress analysis result of the optimum model.

5. Conclusions

This paper suggests the NIA for multimodal optimization. By applying the proposed algorithm and the conventional IA to the test function, outstanding performance of the NIA was verified. The NIA is applied to the optimal design of the IPMSM for FCEVs to diminish torque ripple, considering average torque and cogging torque. By combining the FEM with the NIA, the optimal design result is derived within a significantly reduced computation time, and the torque ripple of the optimized model was decreased by 77.73% compared to the initial model. The proposed algorithm is expected to be widely used in the design of other electrical machines that need to consider various aspects.

Author Contributions: Investigation, J.-C.S. and Y.-R.K.; methodology, J.-C.S. and Y.-R.K.; project administration, D.-K.L.; supervision, D.-K.L.; writing—original draft, J.-C.S.; writing—review and editing, D.-K.L. All authors have read and agreed to the published version of the manuscript.

Funding: This research received no external funding.

Acknowledgments: This work was supported by the National Research Foundation of Korea (NRF) and grant funded by the Korea government (Ministry of Science and ICT) (No. 2019R1F1A1061132).

Conflicts of Interest: The authors declare no conflicts of interest.

References

1. Liu, Y.; Ho, S.L.; Fu, W.; Zhang, X. Design Optimization of a Novel Doubly Fed Dual-Rotor Flux-Modulated Machine for Hybrid Electric Vehicles. *IEEE Trans. Magn.* **2015**, *51*, 1–4. [[CrossRef](#)]
2. Zheng, P.; Liu, Y.; Wang, Y.; Cheng, S. Magnetization analysis of the brushless DC motor used for hybrid electric vehicle. *IEEE Trans. Magn.* **2005**, *41*, 522–524. [[CrossRef](#)]
3. Wu, J.; Wang, J.; Gan, C.; Sun, Q.; Kong, W. Efficiency Optimization of PMSM Drives Using Field-Circuit Coupled FEM for EV/HEV Applications. *IEEE Access* **2018**, *6*, 15192–15201. [[CrossRef](#)]
4. Li, H.; Zhang, X.; Yang, S.; Li, E.; Hong, J. Multi-Objective Controller Design of IPMSM Drives Based on DTD D-Partition Method Considering Parameters Uncertainties. *IEEE Trans. Energy Convers.* **2018**, *34*, 1052–1062. [[CrossRef](#)]
5. Yin, Q.; Li, H.; Luo, H.; Wang, Q.; Xu, C. An Improved Sensorless Vector Control Method for IPMSM Drive with Small DC-Link Capacitors. *Energies* **2020**, *13*, 580. [[CrossRef](#)]
6. Seo, J.-H.; Woo, D.-K.; Chung, T.-K.; Jung, H.-K. A Study on Loss Characteristics of IPMSM for FCEV Considering the Rotating Field. *IEEE Trans. Magn.* **2010**, *46*, 3213–3216. [[CrossRef](#)]
7. Wu, C.; Yang, J.; Li, Q. GPIO-Based Nonlinear Predictive Control for Flux-Weakening Current Control of the IPMSM Servo System. *Energies* **2020**, *13*, 1716. [[CrossRef](#)]
8. Kim, H.-S.; Kwon, B.-I. Optimal design of motor shape and magnetisation direction to obtain vibration reduction and average torque improvement in IPM BLDC motor. *IET Electr. Power Appl.* **2017**, *11*, 378–385. [[CrossRef](#)]
9. Ren, W.; Xu, Q.; Li, Q.; Zhou, L. Reduction of Cogging Torque and Torque Ripple in Interior PM Machines With Asymmetrical V-Type Rotor Design. *IEEE Trans. Magn.* **2016**, *52*, 1–5. [[CrossRef](#)]
10. Lee, J.-G.; Lim, D.-K.; Jung, H.-K. Analysis and Design of Interior Permanent Magnet Synchronous Motor Using a Sequential-Stage Magnetic Equivalent Circuit. *IEEE Trans. Magn.* **2019**, *55*, 1–4. [[CrossRef](#)]
11. Watanabe, K.; Campelo, F.; Igarashi, H. Topology Optimization Based on Immune Algorithm and Multigrid Method. *IEEE Trans. Magn.* **2007**, *43*, 1637–1640. [[CrossRef](#)]
12. Chun, J.-S.; Jung, H.-K.; Hahn, S.-Y. A study on comparison of optimization performances between immune algorithm and other heuristic algorithms. *IEEE Trans. Magn.* **1998**, *34*, 2972–2975. [[CrossRef](#)]
13. Boccaletti, C.; Elia, S.; Nistico, E. Deterministic and stochastic optimisation algorithms in conventional design of axial flux PM machines. In Proceedings of the International Symposium on Power Electronics, Electrical Drives, Automation and Motion, SPEEDAM 2006, Taormina, Italy, 23–26 May 2006.
14. Zhu, J.; Cheng, K.W.E.; Xue, X.; Zou, Y. Design of a New Enhanced Torque In-Wheel Switched Reluctance Motor with Divided Teeth for Electric Vehicles. *IEEE Trans. Magn.* **2017**, *53*, 2070–2073. [[CrossRef](#)]
15. Lim, D.-K.; Yi, K.-P.; Jung, S.-Y.; Jung, H.-K.; Ro, J.-S.; Dong-Kuk, L. Optimal Design of an Interior Permanent Magnet Synchronous Motor by Using a New Surrogate-Assisted Multi-Objective Optimization. *IEEE Trans. Magn.* **2015**, *51*, 1–4. [[CrossRef](#)]
16. Tang, Q.; Shen, A.; Luo, P.; Shen, H.; Li, W.; He, X. IPMSMs Sensorless MTPA Control Based on Virtual q-Axis Inductance by Using Virtual High-Frequency Signal Injection. *IEEE Trans. Ind. Electron.* **2020**, *67*, 136–146. [[CrossRef](#)]
17. Hong, G.; Wei, T.; Ding, X. Multi-Objective Optimal Design of Permanent Magnet Synchronous Motor for High Efficiency and High Dynamic Performance. *IEEE Access* **2018**, *6*, 23568–23581. [[CrossRef](#)]
18. Kim, D.-W.; Park, G.-J.; Lee, J.-H.; Kim, J.-W.; Kim, Y.-J.; Jung, S.-Y. Hybridization Algorithm of Fireworks Optimization and Generating Set Search for Optimal Design of IPMSM. *IEEE Trans. Magn.* **2017**, *53*, 1–4. [[CrossRef](#)]
19. Goto, H.; Sato, M.; Guo, H.; Ichinokura, O. A Simple Method to Reduce Torque Ripple of SR Motors using Freewheeling mode for Electric Vehicles. In Proceedings of the 2006 IEEE International Magnetism Conference (INTERMAG), San Diego, CA, USA, 8–12 May 2006.
20. Hao, J.; Suo, S.; Yang, Y.; Wang, Y.; Wang, W.; Chen, X. Optimization of Torque Ripples in an Interior Permanent Magnet Synchronous Motor Based on the Orthogonal Experimental Method and MIGA and RBF Neural Networks. *IEEE Access* **2020**, *8*, 27202–27209. [[CrossRef](#)]
21. Fang, L.; Kim, S.-I.; Kwon, S.-O.; Hong, J.-P. Novel Double-Barrier Rotor Designs in Interior-PM Motor for Reducing Torque Pulsation. *IEEE Trans. Magn.* **2010**, *46*, 2183–2186. [[CrossRef](#)]

22. Gwak, S.Y. Characteristic Analysis and Design of Multi-Layer Buried Permanent Magnet Motor for Vehicle Traction. Ph.D. Thesis, Seoul National University, Seoul, Korea, 2008.
23. Chu, G.; Dutta, R.; Rahman, M.; Lovatt, H.C.; Sarlioglu, B. Analytical Calculation of Maximum Mechanical Stress on the Rotor of Interior Permanent-Magnet Synchronous Machines. *IEEE Trans. Ind. Appl.* **2020**, *56*, 1321–1331. [[CrossRef](#)]
24. Chai, F.; Li, Y.; Liang, P.; Pei, Y. Calculation of the Maximum Mechanical Stress on the Rotor of Interior Permanent-Magnet Synchronous Motors. *IEEE Trans. Ind. Electron.* **2016**, *63*, 3420–3432. [[CrossRef](#)]



© 2020 by the authors. Licensee MDPI, Basel, Switzerland. This article is an open access article distributed under the terms and conditions of the Creative Commons Attribution (CC BY) license (<http://creativecommons.org/licenses/by/4.0/>).